

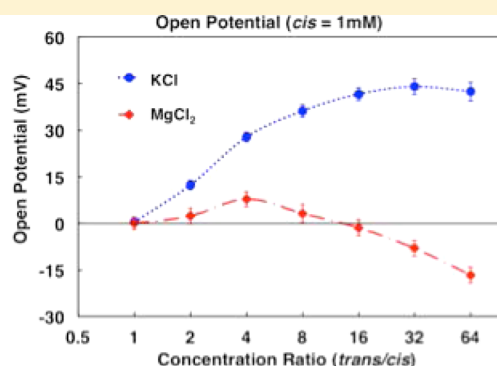
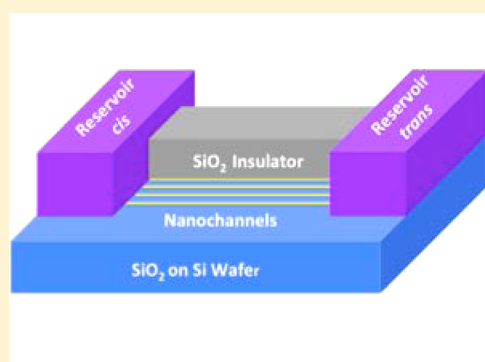
Direct Observation of Charge Inversion in Divalent Nanofluidic Devices

Sylvia Xin Li,^{*,†} Weihua Guan,[§] Benjamin Weiner,[†] and Mark A. Reed^{*,‡}

[†]Department of Physics and [‡]Department of Electrical Engineering & Applied Physics, Yale University, New Haven, Connecticut 06520, United States

[§]Department of Electrical Engineering, Pennsylvania State University, State College, Pennsylvania 16801, United States

S Supporting Information



ABSTRACT: Solid-state nanofluidic devices have proven to be ideal systems for studying the physics of ionic transport at the nanometer length scale. When the geometrical confining size of fluids approaches the ionic Debye screening length, new transport phenomena occur, such as surface mediated transport and permselectivity. Prior work has explored these effects extensively in monovalent systems (e.g., predominantly KCl and NaCl). In this report, we present a new characterization method for the study of divalent ionic transport and have unambiguously observed divalent charge inversion at solid/fluid interfaces. This observation has important implications in applications ranging from biology to energy conversion.

KEYWORDS: Nanofluidics, charge inversion, divalent ion transport, open potential, ion–ion correlation

Nanofluidics has been a rich domain of increasing scientific and technological interest, with a broad range of applications such as ionic and molecular control, energy conversion and storage, and filtration and desalination.^{1–3,5,29} With dimensional miniaturization, intriguing new transport properties appear due to strong surface effects, especially when the Debye lengths of neighboring interfaces start to overlap.^{4,7,8} Most of the previous work in the field of nanofluidics has predominantly focused on simple monovalent electrolytes (e.g., KCl and NaCl), which can be conceptualized with mean-field theory (Poisson–Boltzmann equation).^{7,8} However, mean-field theory alone is no longer valid in multivalent systems where ion–ion correlations are too strong to be neglected.^{9,15}

In particular, charge inversion has been widely discussed in recent years, due to its critical role in many biological and chemical processes such as DNA condensation, viral packaging, and colloidal coagulation.^{9,14–21} Devices with unique performances such as diode junctions have been developed utilizing local charge inversion.^{32–34} Charge inversion happens at a critical concentration when the surface charge at solid/fluid interfaces inverts its sign as a result of overscreening by counterions in the solution. To explain this counterintuitive effect, it has been suggested that a strongly correlated liquid

(SCL) layer forms at the interface where electrostatic interactions are dominant.¹⁵ Streaming current measurements and AFM force detection have supported the SCL theory in high valence regimes (trivalent/quadrivalent).^{20,21} However, there are unclear discrepancies between theory and experiment in the divalent regime.^{15,20} Prior experiments in the divalent regime have reported critical charge inversion concentrations an order of magnitude above the prediction from SCL theory.²⁰ However, the sensitivity of the methods used in these experiments may not have been sufficient to detect divalent charge inversion at lower concentrations. As a result, there is ambiguity as to whether SCL theory is valid for divalent ions, and other theories have been developed to reconcile these findings.⁴²

Determining the physics underlying divalent systems is an important step to understanding biological systems.¹¹ It is speculated that multivalent ions are involved in nucleic acid folding; in particular, divalent Mg²⁺ is essential in RNA folding.^{13,14,40} The failure of simple electrostatics and mean-

Received: March 21, 2015

Revised: May 28, 2015

Published: June 23, 2015

field theories to explain the role of Mg^{2+} in RNA folding indicates that ion–ion correlations may be responsible^{43,44} and raises the possibility that divalent charge inversion may play a role in nucleic acid folding. The discrepancies for when, or even if, charge inversion occurs for divalent ions motivates us to develop a model system to observe and quantify divalent charge inversion under well controlled conditions. To clearly elucidate the physics of divalent charge inversion, we have implemented an effective and facile method of open potential measurement in magnesium ion solutions. This open potential measurement in nanochannels has the advantage of being very sensitive to the change of surface charge, due to the Debye lengths overlap in a confined geometry. Using this approach, we observed a clear signature of charge inversion in a divalent system and the critical concentration falls in the range of SCL theoretical prediction. Our solid-state nanochannels with well-defined geometry provide a unique experimental platform that amplifies surface effects and enables in-depth exploration of divalent ion–surface interaction.

Results. Device Schematic. The schematic structure of the nanochannel fluidic device is illustrated in Figure 1. The devices are fabricated using standard semiconductor fabrication techniques. Photolithographically patterned chromium nano-wires, which define the geometrical dimensions, are buried in SiO_2 and sacrificially etched in the last step after bonding with microfluidic inputs and outputs. The microfluidic channels connect the nanochannels to fluidic reservoirs at each end (defined as *cis* and *trans*). To enable low conductance measurements, a parallel array of identical nanochannels are utilized. Detailed fabrication processes can be found in prior publications^{23,25} and in the Methods section.

Open Potential Measurement. As depicted in Figure 1b, the surface charge of the nanochannel causes counterions to be attracted to the charged interfaces, whereas co-ions are expelled. This electrostatic interaction with the surface charge results in the enrichment of counterions, and exclusion of co-ions when the nanochannel dimension is on the order of Debye length, thus forming asymmetric ionic concentration profiles inside the nanochannel, leading to permselectivity.^{10,26,28} To characterize such permselectivity of nanochannels more precisely than using Debye lengths, a dimensionless Dukhin number $D_u = \sigma/Fhzc_0$ can be introduced, which approximates the ratio of surface conductivity to bulk conductivity.⁴⁵ Here F , h , z , c_0 , and σ are the Faraday constant, the channel height, the valence, the ion concentration outside electrical double layer, and the surface charge inside nanochannels. When $D_u \gg 1$, the surface effect starts to dominate and the nanochannel becomes permselective, whereas in the case of $D_u \ll 1$ the nanochannel will exhibit bulk solution behavior (Figure 1a).

When concentrations at the reservoirs *cis* and *trans* are different, a voltage difference (the open potential, or membrane potential) arises due to electrostatic interactions and diffusion.⁶ The sign as well as the magnitude of the open potential is determined by the net surface charge. The open potential can be described via the membrane potential equation:

$$\Phi = (2t_+ - 1) \frac{RT}{F} \ln \alpha \quad (1)$$

where α is the concentration ratio of two reservoirs, F is the Faraday constant, and RT is the product of the molar gas constant and the room temperature (295 K).³ The cation transport number t_+ is denoted by the fraction of total current carried by cations inside the nanochannel. For a concentration

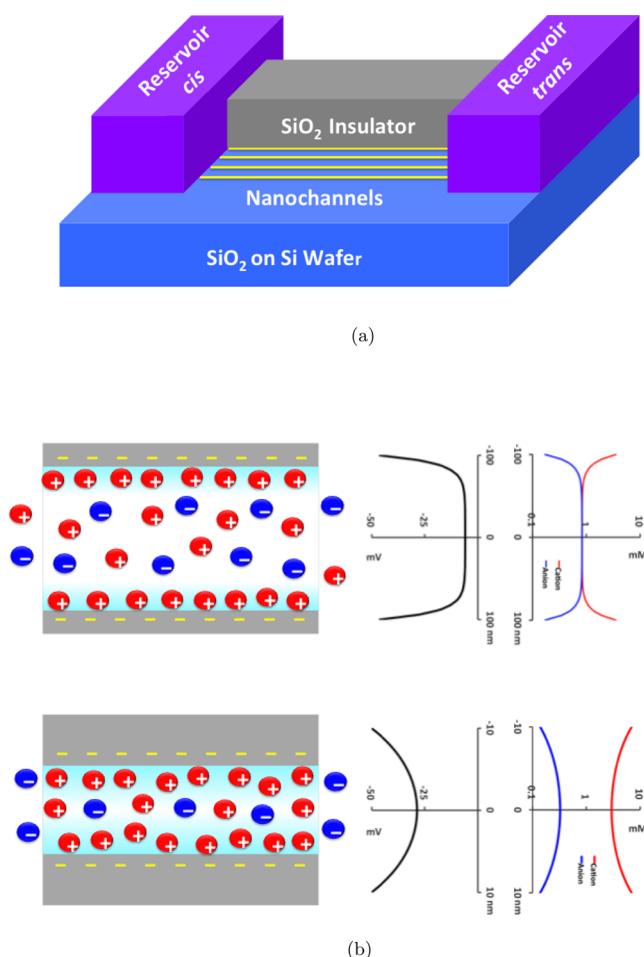


Figure 1. (a) Device schematic of 20 nm high, 11 μm wide, and 116 μm long nanochannels encompassed by SiO_2 ; the two ends of a nanochannel are connected to bulk reservoirs *cis* and *trans*. (b) A demonstration to compare ionic distributions in channels with different height, where the top diagram illustrates a 200 nm high channel and the bottom diagram illustrates a 20 nm high channel; along the height of the channels, the black, red, and blue curves show the distributions of potential, cation concentration and anion concentration, respectively. The distributions are obtained by numerical simulation with the same negative constant surface charge as well as the same bulk concentration of 1 mM KCl.

ratio of 10 and a cation transport number $t_+ = 1$, the open potential at 295 K would be around 58 mV. In the case of KCl, t_+ is just the percentage of cation concentration among total ion concentrations, due to the similar diffusion coefficients of K^+ and Cl^- . For divalent AB_2 solutions, the membrane potential Φ needs to be modified to take into account the diffusion coefficients of different ionic species:

$$\Phi = (1.5t_+ - 1) \frac{RT}{F} \ln \alpha \quad (2)$$

where the transport number $t_+ = 4D_A C_A / (4D_A C_A + D_B C_B)$ is determined by both the diffusion coefficients (D) and ionic concentrations (C).^{37,38} Since the net surface charge determines the cation transference number t_+ , open potential measurements directly reveal the net surface charge. The open potential will reverse sign when $2t_+ - 1$ (monovalent case) or $1.5t_+ - 1$ (divalent case) is smaller than zero, indicating a change in the sign of the net surface charge.

Figure 2a compares monovalent KCl with divalent MgCl_2 in terms of the open potential versus the concentration ratio, both

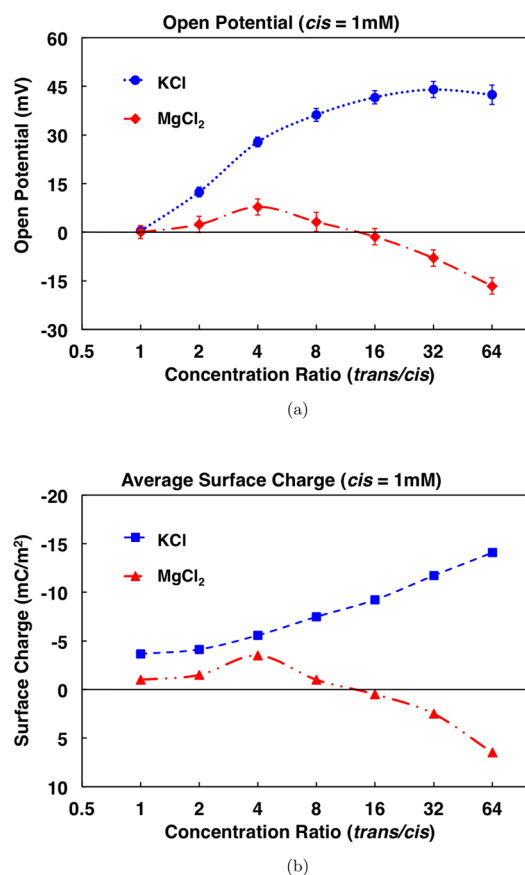


Figure 2. (a) Open potential measurement of KCl (blue) and MgCl_2 (red) versus the reservoir concentration ratio *trans/cis*. While the reservoir *cis* has the fixed concentration of 1 mM, the other end *trans* has varying concentrations from 1 to 64 mM in binary logarithm, corresponding to concentration ratio of 1 to 64. (b) The average surface charge inside the nanochannels obtained by numerical calculation with COMSOL script environment from the open potential measurements in (a); the blue and red lines represent KCl and MgCl_2 , respectively. The surface charge for MgCl_2 starts to invert sign when the concentration ratio exceeds 8, whereas the surface charge for KCl stays negative.

with the *cis* reservoir fixed at 1 mM. In the monovalent case, the increasing concentration ratio simply causes an increase in open potential, whereas in the divalent case a reversal of the sign of the open potential is observed. From the measured open potentials, we can calculate the average net surface charge, which is plotted in Figure 2b. The expected increasing trend of the net surface charge magnitude is observed for monovalent KCl. This is mainly due to the change of local pH inside the nanochannel, which influences the surface chemistry of SiO_2 walls (see details in Supporting Information). The net surface charge values of KCl solutions from our experiment are also in good agreement with previously published results.³¹ For divalent MgCl_2 , however, the sign of the average net surface charge is reversed from negative to positive when the concentration ratio exceeds 8, providing a direct evidence of the overscreening effect, namely, charge inversion.

To explain this counterintuitive phenomenon, it has been suggested that a strongly correlated liquid (SCL) layer forms at the channel/fluid interface, where additional high valence ions

arriving at a neutral surface repel adsorbed ones, creating a correlation hole, in other words, a negative image.¹⁵ The SCL layer is characterized by a large negative chemical potential and attracts additional counterions to the surface due to these lateral correlations.¹⁵ This explanation predicts a critical concentration at which charge inversion happens (detailed discussion in Supporting Information). In Figure 3, the net

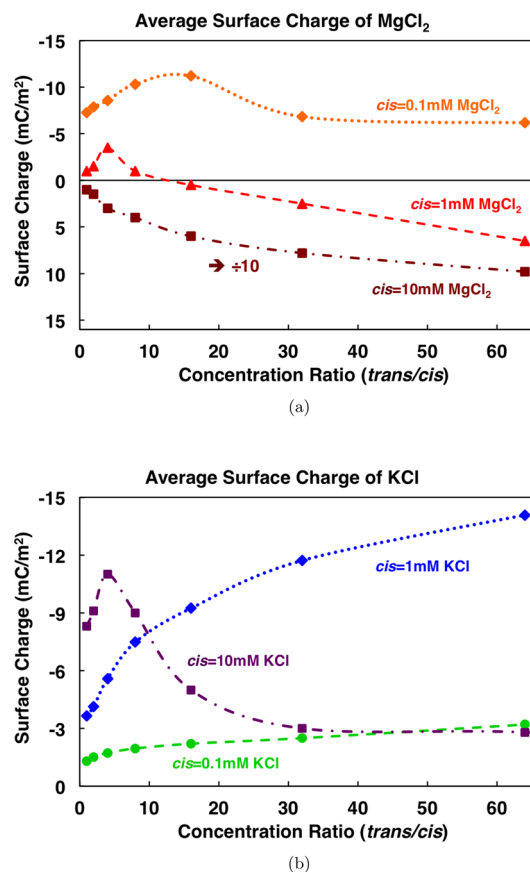


Figure 3. (a) The average surface charge obtained from numerical simulation for MgCl_2 with *cis* concentrations of 0.1, 1, and 10 mM; the plotted 10 mM surface charge values are divided by 10 to fit in the same graph. The *cis* = 0.1 mM trend shows negative surface charge before charge inversion, whereas the *cis* = 10 mM trend reveals that the reversed surface charge continues to increase with growing concentration ratio after charge inversion. (b) The average surface charge obtained from numerical simulation for KCl with *cis* concentrations of 0.1, 1, and 10 mM. All surface charges stay negative and charge inversion does not happen.

average surface charge derived from open potential measurements is plotted versus *trans/cis* concentration ratios (i.e., similar to Figure 2b), but now with different initial *cis* concentrations. In Figure 3a for MgCl_2 , the net average surface charge does not change sign (although the onset of screening is seen) when the *cis* concentration is 0.1 mM (and a maximum *trans* concentration of 6.4 mM); when the *cis* concentration is 10 mM, the net average surface charge is already inverted with low concentration ratio of 2, and its magnitude continues to increase with increasing concentration ratios. These measurements are consistent with the previous open potential measurement, which reveals the critical concentration of ~ 10 mM MgCl_2 . In Figure 3b, we present the same measurements for monovalent KCl. In this case, the net surface charge has the

same sign (always negative) regardless of the concentrations. At the highest concentrations (*cis* = 10 mM; *trans* maximum = 0.64 M), although significant screening occurs, the surface charge for KCl never inverts. (To confirm this, an extremely high 1 M *trans* concentration is applied while *cis* = 10 mM, with a measured open potential of 1 ± 1 mV.) We note that the onset of screening (when the surface charge starts to decrease) occurs at a much higher concentration for monovalent KCl (~40 mM) than the divalent MgCl_2 (~1 mM). However, when the MgCl_2 concentration is increased such that the bare surface charge is overscreened and the net surface charge changes sign (~10 mM), the same increase of KCl concentration does not cause charge inversion.

Conductance Measurement. Additional insights into the surface charge can be gained with a different approach: ionic conductance measurement through the nanochannels with equal *trans* and *cis* concentrations. The measurement of ionic conductivity through nanochannels typically has two different regimes.^{27,28} At high concentrations, the Debye length is much smaller than the channel width, so conductivity through the nanochannel is determined by the bulk conductivity of the ionic solution. At low concentrations, the channel conductivity is dominated by the surface charge due to the overlap of Debye lengths (Figure 1b, bottom) and is therefore concentration independent. A simple interpretation of these effects can be described, assuming constant ionic mobility and constant net surface charge, by

$$G = Ze(\mu_{\text{cation}} + \mu_{\text{Cl}})CN_A WH/L + 2\sigma\mu_{\text{cation}} W/L \quad (3)$$

Here Z , N_A , and C are the cation valence, the Avogadro number, and the reservoir concentration. μ_{cation} and μ_{Cl} are the cation and anion mobility, respectively. At low concentrations, the first term of bulk behavior in the above equation becomes negligible and the second term of surface effects begins to dominate. Since the surface contribution is only related to the net surface charge σ and the cation mobility μ_{cation} inside the channel, the conductance exhibits a saturation plateau regardless of the concentration.^{27,28} Figure 4 shows the measured nanochannel conductivity (solid dots) versus concentration (*cis* = *trans*), showing two different regimes for both KCl and MgCl_2 . The dashed lines are a best fit using the constant ionic mobility and constant net surface charge model. We see that the low concentration plateau conductance value of MgCl_2 is larger than the conductance of KCl, while the Mg^{2+} mobility is smaller than K^+ (around 70%), indicating the surface charge of MgCl_2 is approximately three times the surface charge of KCl. This is consistent with results from open potential measurements in the low concentration range, which reveal a similar difference in the average net surface charge density between MgCl_2 and KCl in Figure 3 (i.e., *cis* = 0.1 mM).

However, there are some large discrepancies between the dashed line fit and the experimental data seen in both KCl and MgCl_2 cases at low concentrations. The inset to Figure 4 exhibits a magnification of the low concentration region, showing the simple constant ionic mobility and constant net surface charge model (dashed lines), and an improved model (solid lines) incorporating additional contributions of proton transfer and concentration-dependent net surface charge. We utilize a numerical model to self-consistently calculate the net surface charge not only in the presence of the cation and anion species, but also taking into account SiOH dissociation dependent on the local proton concentration.^{30,31,39} In addition, the Poisson–Nernst–Planck equation is solved to

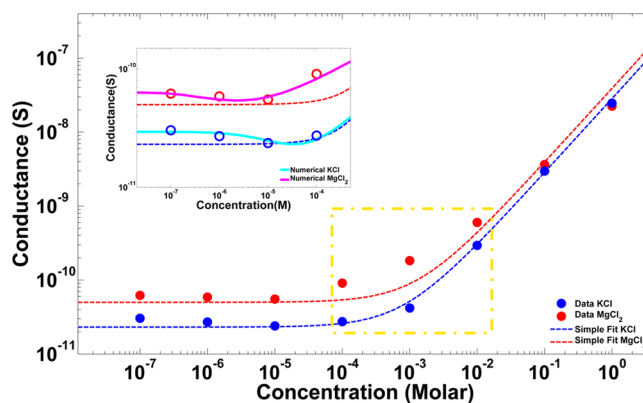


Figure 4. Measured conductance data for KCl (blue) and MgCl_2 (red) are in solid dots; the dashed lines are the simple fit with a constant mobility and constant surface charge model for KCl (blue) and MgCl_2 (red). Zoomed in to the low concentration conductance plateau area, the inset graph shows the experimental data of KCl (blue circles) and MgCl_2 (red circles), and the simple fit (dashed lines). The numerical fit (solid lines) is an improved model taking into account the change of surface charge and proton contribution to low concentration conductance. The numerical model with solid lines (light blue for KCl and magenta for MgCl_2) fits the experimental data well, whereas the simple fit in dashed lines has large discrepancy from the measured values. The transition region where charge inversion happens between high concentration and low concentration is highlighted by yellow dashed lines; increased conductivity of divalent MgCl_2 is observed in this region.

calculate the concentration of every ion species (cation, anion, proton, and HCO_3^-) and thus obtaining a more accurate conductivity. Proton plays an important role in the extremely low concentration region. Since the bulk cation concentration is comparable or even smaller than proton concentration, the local proton concentration inside nanochannels is no longer neglectable. The overall conductivity is therefore decided by three factors: change of surface charge, cation concentration, and proton concentration inside the nanochannel.

In the extremely low (0.01 mM and below) concentration region, the revised model fits the data well, mainly due to the proton conductivity. For KCl at this concentration range, the change of surface charge versus concentration is insignificant. However, the surface charge does change significantly for MgCl_2 using the same model. This can be observed in the point of minimum conductance: for KCl it is mid 10^{-5} M, whereas for MgCl_2 it is mid 10^{-6} M. It is also noted that the conductance behavior in this extremely low concentration region is self-consistent with the assumption of constant ion mobility, in contrast to previously reported results.³¹ The changing trends of surface charge of both KCl and MgCl_2 is plotted in Figure S5 in the Supporting Information.

In the high concentration regime, when $|s| \ll eCH$, the surface contribution $2\sigma\mu_{\text{cation}}W/L$ is negligible.²⁷ The conductance behavior of KCl is well described by the constant mobility model, whereas the MgCl_2 conductance deviates considerably from the constant mobility model. To explain this deviation, we have performed detailed measurements of the bulk conductance of MgCl_2 .³⁶ It is found that the nano/bulk conductance ratio is almost 1 for MgCl_2 at concentrations $\geq 0.1\text{M}$, and the decreasing molar conductivity is an intrinsic characteristic of MgCl_2 .³⁶ A possible explanation is ion mobility correlation.³⁵ The nano/bulk conductance ratios are presented in Figure S6 in the Supporting Information.

An interesting behavior occurs in the transition region from bulk conductance to surface-dominated conductance plateau. At high concentration, the channel conductance is almost the same as the bulk for $C \geq 100$ mM, when accounting for the concentration-dependent conductivity. At low concentrations, the conductivity is described by concentration-independent surface charge dominated transport (described previously). However, in the transition region from 1 to 10 mM, there is an anomalous increase of conductance for MgCl_2 (highlighted by the yellow dashed line in Figure 4). This transition region coincides with the concentration range where charge inversion is observed. The open potential measurement of $cis = 1$ mM series of MgCl_2 reveals that the net surface charge is very small and even reverses sign at around 10 mM. Accordingly, the surface-charge dominated transport term is very small (or even vanishes). The anomalously high conductivity in the inversion charge regime is not understood at present, although one possible explanation is that the highly condensed two-dimensional SCL layer at the surface is conductive and contributes to the conductance.

Conclusions. Utilizing an effective method of open potential and conductance measurement, we have systematically studied divalent ion transport in nanochannels. We have observed a clear signature of divalent charge inversion in MgCl_2 solution and anomalous increase of its conductivity in the region of charge inversion. Such complex interplay of surface–ion interaction and electrostatic correlation are crucial in many chemical and biological processes such as colloidal assembly,⁴¹ DNA condensation,⁴⁴ and RNA folding.¹³ Our device structure also allows for the control of surface chemistry by functionalization and the modification of surface potential by electric field gating for future study.^{22,24} In addition, magnesium-based batteries have attracted increasing attention in recent years.¹² The charge inversion phenomenon of magnesium ions at solid/fluid interfaces may shed light on understanding the difficulty of magnesium-insertion in cathode materials, and the observed increase of nanoscale conductivity may help design more efficient battery structures. In conclusion, our study of the basic physics of divalent ion transport under nanoscale confinement may have implications in fields such as biophysics, colloidal science, and energy conversion.

Methods. Device Fabrication. First, a sacrificial layer of chromium ($H = 20$ nm) is deposited on SiO_2 , and nanowire structures ($L = 116$ μm , $W = 11$ μm) are patterned by photolithography in the chromium layer. The chromium nanowires are then buried in PECVD (plasma-enhanced chemical vapor deposition) SiO_2 and etched through in the last step by chromium etchant after bonding with PDMS (polydimethylsiloxane, silicon-based organic polymer). The Cr etchant is pumped into the microfluidic channels inside the PDMS layer and rinsed thoroughly by DI water when the etching is finished. The color of the channels will change under microscope after etching, and the KCl conductance measurement further proves that the channels are etched thoroughly. Geometrically well-defined nanochannels are thus formed with robust solid-state SiO_2 walls. Connected to the two ends of a nanochannel, there are 200 μm wide and 1000 μm long micropillar areas with pillar height of ~ 3 μm . These micropillar areas overlap with microfluidic channels in the PDMS layer, which lead to holes in PDMS where Ag/AgCl electrodes are inserted. The aqueous solutions flow along microfluidic channels inside PDMS and diffuse into the nanochannels by

passing micropillar reservoirs (Figure S1 in the Supporting Information).

Measurements. The open potential is measured by an electrometer, Keithley 6514. All the open potentials are plotted in Figure S2 in the Supporting Information. For conductance, the current is measured by an electrometer Keithley 6514, while the voltage sweep is applied by a voltage source Keithley 230 at step size 0.1 V from -0.5 to 0.5 V. Each data point is repeated at least three times. All electric measurements are done in a Faraday box at room temperature, 295 K. The bulk conductivity of KCl and MgCl_2 solutions are measured by a conductivity meter EC215 from Hanna Instrument. The nano/bulk conductivity ratios are presented in Figure S6 in the Supporting Information.

Numerical Simulations. Numerical simulations are realized by solving coupled Poisson–Nernst–Planck equation and surface dissociation equation in COMSOL script environment. Electrostatics module and diluted species transport module for each ion species are introduced in COMSOL. The simulated system is defined in two-dimensional area with a 20 nm high and 5 μm long channel connected to 3 μm square reservoirs. Detailed description is in the Supporting Information.

■ ASSOCIATED CONTENT

Supporting Information

Device setup, pH measurement, open potential measurements and error analysis, numerical model, conductance measurements and error analysis, and strongly correlated liquid theory. The Supporting Information is available free of charge on the ACS Publications website at DOI: 10.1021/acs.nanolett.5b01115.

■ AUTHOR INFORMATION

Corresponding Authors

*E-mail: xin.li.xl288@yale.edu.

*E-mail: mark.reed@yale.edu.

Notes

The authors declare no competing financial interest.

■ ACKNOWLEDGMENTS

This research was supported as part of Nanostructures for Electrical Energy Storage (NEES), an Energy Frontier Research Center funded by US Department of Energy (DOE), Office of Science, Office of Basic Energy Sciences (BES) under Award No. DESC000160. We also acknowledge the Yale Institute for Nanoscience and Quantum Engineering and NSF MRSEC DMR 1119826. We appreciate the help from Mike Power, Chris Tillinghast, and Shari Yosinski in cleanroom fabrication, and the discussion with Luye Mary Mu on the manuscript.

■ REFERENCES

- (1) Kim, S. J.; Ko, S. H.; Kang, K. H.; Han, J. *Nat. Nanotechnol.* **2010**, 5, 297.
- (2) van der Heyden, F. H. J.; Bonthuis, D. J.; Stein, D.; Meyer, C.; Dekker, C. *Nano Lett.* **2006**, 6, 2232.
- (3) Guan, W.; Li, S. X.; Reed, M. A. *Nanotechnology* **2014**, 25, 122001.
- (4) Bocquet, L.; Tabeling, P. *Lab Chip* **2014**, 14, 3143.
- (5) Siria, A.; Poncharal, P.; Bianco, A. L.; Fulcrand, R.; Blase, X.; Purcell, S. T.; Bocquet, L. *Nature* **2013**, 494, 455.
- (6) Hills, G. J.; Jacobs, P. W. M.; Lakshminarayanaiah, N. *Proc. R. Soc. London, Ser. A* **1961**, 262, 246.
- (7) Daiguji, H. *Chem. Soc. Rev.* **2010**, 39, 901.

- (8) Schoch, R.; Han, J.; Renaud, P. *Rev. Mod. Phys.* **2008**, *80*, 839.
- (9) Grosberg, A. Y.; Nguyen, T. T.; Shklovskii, B. I. *Rev. Mod. Phys.* **2002**, *74*, 329.
- (10) Plecis, A.; Schoch, R. B.; Renaud, P. *Nano Lett.* **2005**, *5*, 1147.
- (11) Nadler, M. J. S.; Hermosura, M. C.; Inabe, K.; Perraud, A.; Zhu, Q.; Stokes, A. J.; Kurosaki, T.; Kinet, J.; Penner, R.; Scharenberg, A. M.; Fleig, A. *Nature* **2001**, *411*, 590.
- (12) Shterenberg, I.; Salama, M.; Gofer, Y.; Levi, E.; Aurbach, D. *MRS Bull.* **2014**, *39*, 453.
- (13) Das, R.; Travers, K. J.; Bai, Y.; Herschlag, D. *J. Am. Chem. Soc.* **2005**, *127*, 8272.
- (14) Besteman, K.; van Eijk, K.; Lemay, S. G. *Nat. Phys.* **2007**, *3*, 641.
- (15) Shklovskii, B. I. *Phys. Rev. E: Stat. Phys., Plasmas, Fluids, Relat. Interdiscip. Top.* **1999**, *60*, 5802.
- (16) Besteman, K.; Zevenbergen, M.; Lemay, S. *Phys. Rev. E* **2005**, *72*, 061501.
- (17) Wernersson, E.; Kjellander, R.; Lyklema, J. *J. Phys. Chem. C* **2010**, *114*, 1849.
- (18) Gurnev, P. A.; Bezrukov, S. M. *Langmuir* **2012**, *28*, 15824.
- (19) Tan, Q.; Zhao, G.; Qiu, Y.; Kan, Y.; Ni, Z.; Chen, Y. *Langmuir* **2014**, *30*, 10845.
- (20) van der Heyden, F.; Stein, D.; Besteman, K.; Lemay, S.; Dekker, C. *Phys. Rev. Lett.* **2006**, *96*, 224502.
- (21) Besteman, K.; Zevenbergen, M. A. G.; Heering, H. A.; Lemay, S. G. *Phys. Rev. Lett.* **2004**, *93*, 170802.
- (22) Guan, W.; Fan, R.; Reed, M. A. *Nat. Commun.* **2011**, *2*, 506.
- (23) Shang, W.; Wang, X.; Yu, Y. *J. Membr. Sci.* **2006**, *285*, 362.
- (24) Guan, W.; Reed, M. A. *Nano Lett.* **2012**, *12*, 6441.
- (25) Nishizawa, M.; Menon, V. P.; Martin, C. R. *Science* **1995**, *268*, 700.
- (26) Schoch, R. B.; van Lintel, H.; Renaud, P. *Phys. Fluids* **2005**, *17*, 100604.
- (27) Stein, D. K. M.; Dekker, C. *Phys. Rev. Lett.* **2004**, *93*, 035901.
- (28) Vlassiuk, I.; Smirnov, S.; Siwy, Z. *Nano Lett.* **2008**, *8*, 1978.
- (29) Hou, X.; Guo, W.; Jiang, L. *Chem. Soc. Rev.* **2011**, *40*, 2385.
- (30) Behrens, S. H.; Grier, D. G. *J. Chem. Phys.* **2001**, *115*, 6716.
- (31) Duan, C. M.; Majumdar, A. *Nat. Nanotechnol.* **2010**, *5*, 848.
- (32) He, Y.; Gillespie, D.; Boda, D.; Vlassiuk, I.; Eisenberg, R. S.; Siwy, Z. *J. Am. Chem. Soc.* **2009**, *131*, 5194.
- (33) Qiao, R.; Aluru, N. R. *Phys. Rev. Lett.* **2004**, *92*, 198301.
- (34) Picallo, C.; Gravelle, S.; Joly, L.; Charlaix, E.; Bocquet, L. *Phys. Rev. Lett.* **2013**, *111*, 244501.
- (35) Hertz, H. G.; Mills, R. J. *Phys. Chem.* **1978**, *82*, 952.
- (36) Phang, S.; Stokes, R. H. *J. Solution Chem.* **1980**, *9*, 497.
- (37) Westermannclark, G. B.; Christoforou, C. C. *J. Electroanal. Chem. Interfacial Electrochem.* **1986**, *198*, 213.
- (38) Hanley, H. J. M. *J. Macromol. Sci., Part B: Phys.* **1969**, *3*, 365.
- (39) Iller, R. K. *Chemistry of Silica*; Wiley: New York, 1979.
- (40) Draper, D. E.; Grilley, D.; Soto, A. M. *Annu. Rev. Biophys. Biomol. Struct.* **2005**, *34*, 221.
- (41) dos Santos, A. P.; Levin, Y. *Phys. Rev. Lett.* **2011**, *106*, 167801.
- (42) Lorenz, C. D.; Travesset, A. *Phys. Rev. E* **2007**, *75*, 061202.
- (43) Anthony, P. C.; Sim, A. Y. L.; Chu, V. B.; Doniach, S.; Block, S. M.; Herschlag, D. *J. Am. Chem. Soc.* **2012**, *134*, 4607.
- (44) Bowman, J. C.; Lenz, T. K.; Hud, N. V.; Williams, L. D. *Curr. Opin. Struct. Biol.* **2012**, *22*, 262.
- (45) Zangle, T. A.; Mani, A.; Santiago, J. G. *Chem. Soc. Rev.* **2010**, *39*, 1014.